ROYAL SOCIETY
OF CHEMISTRY

PAPER

Check for updates

Quasi-1D selenohalides: first-principles insights into thermoelectric and photovoltaic applications

Prakash Govindaraj [ID] and Hern Kim [ID] *

The rapid search for advanced functional materials is increasingly essential to meet the rising global energy demands, secure long-term energy solutions, and achieve a sustainable future. In this work, we systematically investigate the structural, thermoelectric, and photovoltaic properties of quasi-one-dimensional selenohalides XSeHa (X = Sb, Bi; Ha = Cl, Br) using density functional theory. The unique chemical environments, consisting of 1D layers stacked *via* weak van der Waals interactions, give rise to pronounced anisotropic electron and phonon transport properties alongside nearly isotropic optical behavior. The synergistic combination of favorable electronic features and lone-pair electrons yields a high-power factor (1.74 mW m^{-1} K^{-2}) and a low lattice thermal conductivity (0.31 W m^{-1} K^{-1}), resulting in a remarkable thermoelectric figure of merit of up to 0.81 at 600 K for BiSeBr. Additionally, strong optical absorption driven by the imaginary dielectric function and favorable excitonic properties achieves a spectroscopic limited maximum efficiency of 31.13% for SbSeBr. Based on these results, BiSeBr and SbSeBr are suggested as promising candidates for experimental exploration in thermoelectric and photovoltaic applications, respectively. This study not only demonstrates the potential of selenohalides but also provides a thorough assessment of their stability and synthesizability to guide future investigations.

1. Introduction

Eco-friendly energy conversion and storage technologies are being actively developed to address the ongoing energy crisis and mitigate the environmental challenges associated with global warming. In this context, thermoelectric (TE) and photovoltaic (PV) technologies have witnessed remarkable progress in recent years.[1,2] For thermoelectric devices, the efficiency is primarily governed by the dimensionless figure of merit, $zT = \frac{\sigma S^2}{\kappa} T$, where σ is the electrical conductivity, S is the Seebeck coefficient, κ is the total thermal conductivity (the sum of the electronic, κ_e and lattice part, κ_L) and T is the absolute temperature.[3] Typically, $zT > 1$ is considered as a desirable parameter for practical applications. Several Te-based chalcogenides, such as PbTe ($zT = 1.6$ at 773 K), GeTe ($zT = 2.0$ at 700 K), and Bi$_2$Te$_3$ ($zT = 1.4$ at 380 K)[4–6] already demonstrate high performance. Despite these achievements, the scarcity and high cost of Te hinder large-scale commercialization, motivating the search for alternative TE materials composed of earth-abundant elements.[7] In recent years, the discovery and optimization of such materials have been propelled by both experimental and computational approaches.[8,9] To further enhance zT, two strategies have been widely employed: (i) improving electronic

transport through band structure engineering, resonant level doping, and carrier concentration optimization; and (ii) suppressing lattice thermal conductivity *via* nanostructuring, defect engineering, and grain boundary manipulation.[10,11]

In parallel, extensive efforts have been devoted to improving the solar cell conversion efficiency and enabling effective solar energy harvesting.[12,13] Lead-based halide perovskites have emerged as outstanding photovoltaic absorbers due to their high absorption coefficients and exceptional conversion efficiencies, which now exceed 26%. However, their intrinsic toxicity and limited long-term chemical and thermal stability disturb their large-scale commercialization.[14] Other classes of perovskites have also contributed significantly to photovoltaics; for example, the overall efficiency of this family has improved by nearly 47%, from 14.1% in 2013 to 26.95% in 2025. Current research strategies primarily focus on enhancing the open-circuit voltage, improving stability, and optimizing interfacial engineering between the solar absorber and charge-transport layers. Beyond these experimental approaches, first-principles methods and high-throughput computational screening are playing a central role in accelerating materials discovery and deepening the understanding of structure–property relationships, thereby advancing both TE and PV technologies.[15,16]

Multi-anion chalcohalides represent an emerging class of semiconductors with promising potential in energy-related technologies, owing to their inherent properties such as structural tunability, phase stability, and unique electronic features. These materials have been explored for diverse applications,

Department of Energy Science and Technology, Environment Waste Recycle Institute, Myongji University, Yongin, Gyeonggi-do 17058, Republic of Korea. E-mail: hernkim@mju.ac.kr

including photodetectors, solar cells, and batteries.[17–19] From a structural aspect, they typically consist of one or more metals combined with divalent chalcogens and monovalent halogens. Among them, the orthorhombic SbSI and BiSI have gained considerable attention in recent years.[20–22] Originally reported by E. Dönges in 1950, these compounds have been investigated for nearly 75 years across various functional applications, with a predominant focus on their electronic and optical properties.[23] More recently, Chauhan *et al.* examined Janus antimony chalcohalide monolayers for piezoelectric, thermoelectric, photovoltaic, and photocatalytic applications, while Bafekry *et al.* studied the optical and thermoelectric properties of 2D SbXY (X = Se, Te; Y = Br, I).[24,25] However, most of the existing studies emphasize the optical properties of low-dimensional chalcohalides, whereas the thermoelectric and photovoltaic characteristics of their parent bulk quasi-1D analogues, XSeHa (X = Sb, Bi; Ha = Cl, Br), remain largely unexplored to the best of our knowledge.

To address this research gap, we present a detailed investigation on the thermoelectric and photovoltaic properties of quasi-one-dimensional selenohalides within the framework of density functional theory (DFT). This study not only explores the structure–property relationships relevant to thermoelectric and photovoltaic applications but also examines the structural peculiarities, diverse stability aspects, and synthesizability that are critical for guiding experimental realization. These factors are comprehensively analyzed to establish a reliable foundation for practical implementation. For clarity, the paper is organized as follows: Section 2 outlines the computational methodology; Section 3 presents the results and discussion, covering structural, stability, and electronic properties (Sections 3.1–3.3), thermoelectric response (Section 3.4), and photovoltaic performance (Section 3.5); and Section 4 concludes with the key findings and outlook.

2. Computational methods

2.1. First-principles calculations

All the density functional theory (DFT) calculations were performed using the Vienna *Ab initio* Simulation Package (VASP) under the projector augmented wave (PAW) method.[26,27] To treat the core and valence electrons, the Perdew, Burke, and Ernzerhof (PBE) functional under generalized gradient approximation was used.[28] The van der Waals (vdW) dispersion term (DFT-D3) with Becke-Johnson damping function was used to treat the vdW interlayer interaction.[29] Based on the performed convergence test, a kinetic energy cutoff of 550 eV and a Monkhorst–Pack $5 \times 3 \times 7$ k-mesh was applied.[30] The tight energy and force convergence criteria were set as 1×10^{-8} eV and 1×10^{-7} eV Å^{-1}, respectively. All the crystal structures were picturized using the VESTA package.[31] The electronic structure was plotted using the sumo plotting tool.[32] Furthermore, the LOBSTER code was used for crystal orbital Hamiltonian population analysis.[33] The convex hull and chemical potential calculations were performed using the pydefect code.[34]

2.2. Thermoelectric property calculations

The phonon dispersion spectra were calculated by the finite difference method implemented in the phonopy code.[35,36] The single-point calculations on displaced structures were performed using VASP to obtain second-order interatomic force constants. A $3 \times 1 \times 2$ supercell was utilized for phonon related calculations. And a Monkhorst–Pack $3 \times 3 \times 3$ mesh was applied.[30] The phonon frequencies and normalized eigenvectors were computed. The eigenvectors were obtained from the *band.yaml* output file generated with eigenvector printing enabled (EIGENVECTORS = TRUE). These eigenvectors were post-processed using custom Python scripts to evaluate atom-resolved vibrational contributions based on the squared norms of the eigenvector components, which were subsequently used to construct the projected phonon dispersion plots. Furthermore, the lattice thermal conductivity was computed by solving the full linearized Boltzmann transport equation iteratively using the ShengBTE code.[37] The thirdorder.py script was used to generate the displaced structures.[38] The q-mesh and cutoff radius convergence tests were employed with $\Delta\kappa_L$ of 0.05 W m^{-1} K^{-1}. The electron transport properties were calculated by adopting the highly efficient and reliable AMSET code.[39] Here, the code solves the semiclassical Boltzmann transport equation using the BoltzTraP2 code.[40] Furthermore, the relaxation times of carriers were computed by considering multiple scattering mechanisms, such as acoustic phonons, polar optical phonons and ionized impurities. These calculations were performed by considering deformation potentials, elastic constants and dielectric constants. A converged interpolation factor of 110 was used. BiSeCl was considered as a representative system for all the phonon and electron-related convergence tests, which are given in Fig. S1 and S2 of the SI.

2.3. Photovoltaic property calculations

Considering the larger memory requirements for GW calculations, the frequency-dependent dielectric function and optical absorption spectra were obtained through independent particle approximation (IPA) on the top of PBE-D3. The VASPKIT tool was used to post-process the optical properties of the materials.[41] The widely used Spectroscopic Limited Maximum Efficiency (SLME) approach was utilized to access the maximum radiative limit of energy conversion with respect to thickness.[42]

3. Results and discussion

3.1. Crystal structure and bonding analysis

In this work, four selenohalides with chemical formula XSeHa (X = Bi, Sb; Ha = Cl, Br) are studied, as indicated in Fig. 1(a). These selenohalides crystallize in an orthorhombic structure with the *Pnam* space group (refer to Fig. 1(b)). Experimentally, such selenohalides exhibit a needle-like morphology, which originates from their one-dimensional structural peculiarities *i.e.*, an infinite chain extending along the z-direction.[43,44] These chains comprise repeating units of two distorted square pyramids as depicted in Fig. 1(c). Each pyramid contains one Bi/Sb,

This journal is © The Royal Society of Chemistry 2026

J. Mater. Chem. A, 2026, **14**, 10694–10707 | **10695**

two halide, and three chalcogen atoms. The bond lengths are listed in Table S1 for better comparison. The chalcogen atoms serve as bridging units between pyramids, linking them together to form infinite chains as represented in Fig. 1(d). The chains are held together by weak van der Waals interactions, resulting in pronounced anisotropic behavior in the material's physical properties. The atomic structures were optimized using the DFT-D3 method, which includes dispersion corrections to accurately capture the weak interchain interactions. The relaxed lattice parameters show better agreement with previous theoretical and experimental reports (see Table 1).

To investigate the bonding characteristics of XSeHa, Crystal Orbital Hamiltonian Population (COHP) analysis was performed along with the Electron Localization Function (ELF), as illustrated in Fig. 1(e–h). The COHP method provides insights into the bonding and antibonding interactions between atomic pairs by projecting the Hamiltonian onto the selected orbitals. The integrated COHP (ICOHP) values quantify the bonding strength: higher ICOHP values indicate stronger bonding interactions, while lower values correspond to weaker bonds.[45] Here we have considered all the s, p, and d orbitals for cations and anions. Across all the structures, the ICOHP values for Bi/Sb–Se bonds were notably higher than those for Bi/Sb–Cl/Br bonds, suggesting stronger bonding between the cations and Se compared to the halogen atoms.

The insets of Fig. 1(e–h) show the ELF analysis which complements the COHP results by visualizing regions of electron localization, thereby providing deeper insight into the nature of bonding both within and between chains. The ELF values range from 0 to 1, where values of 0, 0.5, and 1

correspond to no localization, partial localization, and complete localization, respectively. The partial electron localization between Sb/Bi and the chalcogen atoms reveals the covalent bonding character, which is consistent with the high ICOHP values. In contrast, significantly lower electron localization was found between Sb/Bi and the halogen atoms, supporting the interpretation of weaker, possibly more ionic interactions. Additionally, 3D ELF isosurfaces plotted along the (001) plane at an isosurface value of 0.0005 reveal the presence of charge density beneath the square pyramids, indicating the existence of lone pair electrons on the cationic centers (refer to Fig. S3). These lone pairs induce significant distortions in the square pyramidal geometry, resulting in unequal bond lengths between the cations and anions (see Table S1). Such structural asymmetry is often associated with enhanced lattice anharmonicity.[46]
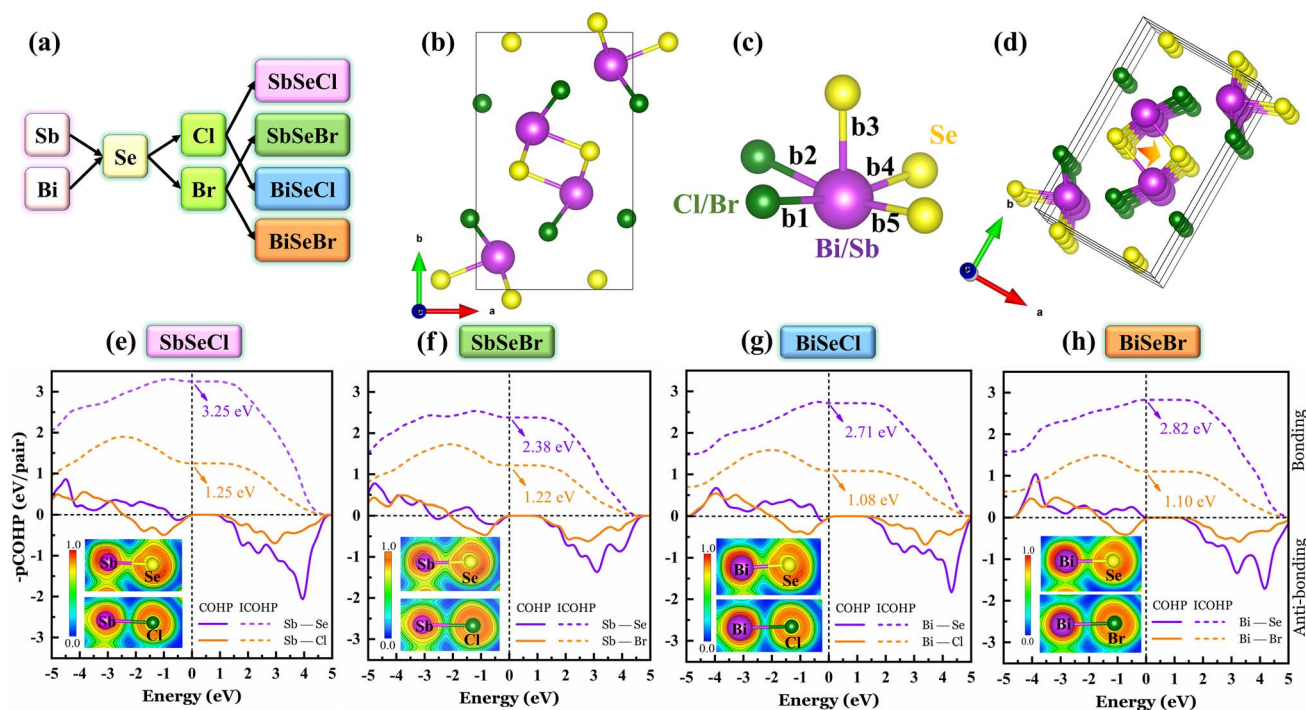
Table 1 Comparison of lattice parameters

| Materials | Lattice parameters (Å) | | | Methods | Reference |
	a	b	c		
SbSeCl	7.554	10.752	3.939	Theo. (PBE + D3)	Present work
SbSeBr	8.275	10.217	3.996	Theo. (PBE + D3)	Present work
	8.300	9.750	3.950	Expt.	47
	8.300	10.200	3.950	—	48
BiSeCl	7.086	11.611	4.005	Theo. (PBE + D3)	Present work
	7.700	9.870	4.000	Expt.	49
BiSeBr	8.220	10.365	4.105	Theo. (PBE + D3)	Present work
	8.180	10.470	4.110	Expt.	23

Fig. 1 (a) Target phases of the present work, (b) crystal structure, (c) square-pyramidal and (d) crystal structure projected along the a direction to capture the chain. The COHP (solid line) and integrated COHP (dashed line) analysis of (e) SbSeCl, (f) SbSeBr, (g) BiSeCl and (h) BiSeBr. Note: insets of Fig. (e–h) represent their respective 2D ELF.

10696 | J. Mater. Chem. A, 2026, 14, 10694–10707

This journal is © The Royal Society of Chemistry 2026

3.2. Phase stability

The combined analysis of the convex hull and chemical potential diagram (CPD) will establish the compound's thermodynamic stability and the permissible synthesis window. Hence, the convex hull and chemical potential diagram (CPD) calculations are carried out, and the results are illustrated in Fig. 2(a–h). The convex hull analysis, Fig. 2(a–d), depicts that the compounds lying on the hull are predicted to be thermodynamically stable. For example, $SbCl_5$, $SbCl_3$, $SeCl_4$, $SbSeCl_9$, SbSeCl and Sb_2Se_3 are found to be stable while constructing convex hull for SbSeCl (refer to Fig. 2(a)). Also, the convex hull illustrates the formation energy of the considered phases. The dark and lighter shades within the different colored convex hull indicate the lower (more favorable) and higher (less favorable) formation energies, respectively. All the selenohalides are observed in the darker shades, except BiSeCl. In the case of BiSeCl, $BiCl_3$ is the most prone phase to be formed during the synthesis process. However, all the interesting selenohalides have negative formation energy from −0.60 to −0.97 eV/atom, indicating their successful formation under experimental conditions. Hence, suitable approaches should be adopted to eradicate the formation of $BiCl_3$ as a secondary phase in BiSeCl synthesis.

Furthermore, the CPDs show the stability window of the selenohalides in terms of the corresponding elemental chemical potentials. The shaded polyhedral regions represent the allowed combinations of chemical potentials where each phase is stable. The targeted selenohalides occupy smaller regions, especially in the case BiSeCl. This reflects their sensitivity to growth conditions, implying that precise control of precursor ratios and the growth environment is required to avoid competing phases.

To facilitate the probability of synthesis, the cohesive energy (E_{coh}) is calculated using the relation $E_{coh}=(E_{PnSeHa} − E_{Pn} − E_{Se} − E_{Ha})/4$, where E_{PnSeHa}, E_{Pn}, E_{Se}, and E_{Ha} represent the energies of the selenohalide and constituent isolated atoms such as pnictogen (Sb/Bi), selenium, and halogen (Cl/Br), respectively.[50] The calculated E_{coh} for SbSeCl, SbSeBr, BiSeCl and BiSeBr is −3.82, −3.68, −3.85 and −3.71 eV/atom, respectively. These values are comparatively higher than those of the experimentally reported chalcohalides like BiSeI (−2.14 eV/atom) which is synthesized by physical vapor deposition and ball milling methods. Hence, it is inferred that these selenohalides can also be synthesized.

To understand the dynamical stability of the selenohalides, the projected phonon dispersion spectra were calculated and
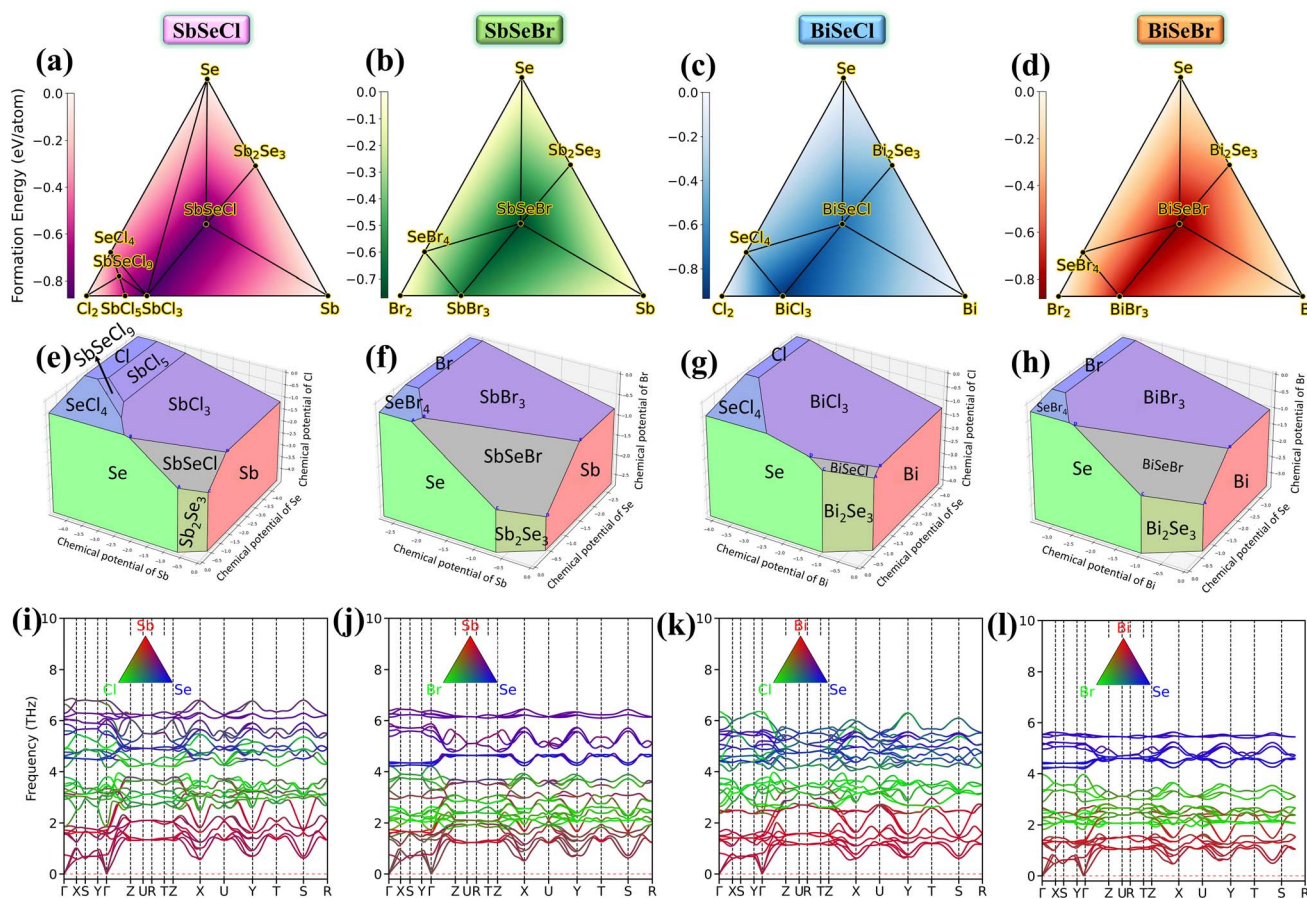

Fig. 2 (a–d) Convex hull diagrams with respect to competing phases. The color variation represents the formation energy, with the corresponding color bar shown on the left side of the diagrams. (e–h) Chemical potential diagrams of the respective competing phases. (i–l) Atom projected phonon dispersion curves. The triangle in the inset shows the atoms corresponding to each color. Figures are arranged in the SbSeCl, SbSeBr, BiSeCl, and BiSeBr sequence (left to right).

This journal is © The Royal Society of Chemistry 2026

J. Mater. Chem. A, 2026, **14**, 10694–10707 | **10697**

Table 2 Calculated elastic constants (C_{ij}, in GPa) of the selenohalides

Elastic constants	SbSeCl	SbSeBr	BiSeCl	BiSeBr
C_{11}	24.08	30.16	23.59	32.35
C_{12}	20.15	19.21	20.08	20.78
C_{13}	13.67	12.87	13.31	14.50
C_{21}	20.15	19.21	20.08	20.78
C_{22}	23.84	24.74	28.02	22.84
C_{23}	15.64	13.29	22.69	16.59
C_{31}	13.67	12.87	13.31	14.50
C_{32}	15.64	13.29	22.69	16.59
C_{33}	68.22	58.71	72.08	56.36
C_{44}	16.87	15.25	18.91	13.95
C_{55}	15.24	12.86	19.36	13.51
C_{66}	6.73	5.42	7.58	4.75

are depicted in Fig. 2(i–l). No imaginary/negative frequency is observed in all the compounds, ensuring their dynamical stability. The unit cell comprises 12 atoms, resulting in 36 phonon modes, including 3 acoustic and 33 optical modes. The highest frequency tends to decrease linearly as the pnictogen/

halogen varies from Cl to Br or Sb to Bi, ascribed to the increasing atomic mass of the corresponding constituent elements. The Sb/Bi, Cl/Br and Se atoms predominantly contribute to the low, mid and high frequency modes respectively. For a specific mode, the highest frequency along different crystallographic directions follows the trend $x < y < z$ for all the selenohalides. For instance, in SbSeCl, the highest frequency of the TA mode is 0.57, 0.69 and 1.38 THz along the x-, y-, and z-directions, respectively. This directional variation in phonon frequencies indicates pronounced anisotropy in phonon transport. In crystalline solids, acoustic phonon modes are the primary contributors to heat conduction due to their abrupt variation in frequency. Notably, the frequencies also vary significantly with respect to q-points, particularly near the Γ-point. Consequently, acoustic modes are expected to contribute significantly to the phonon velocity, which generally correlates with higher κ_L. Additionally, band crossing is avoided between the highest acoustic and lowest optical modes in all the investigated compounds. This feature may reflect the weak bonding characteristics of the crystal, but it could also signify the presence of strong anharmonicity and enhanced phonon–phonon
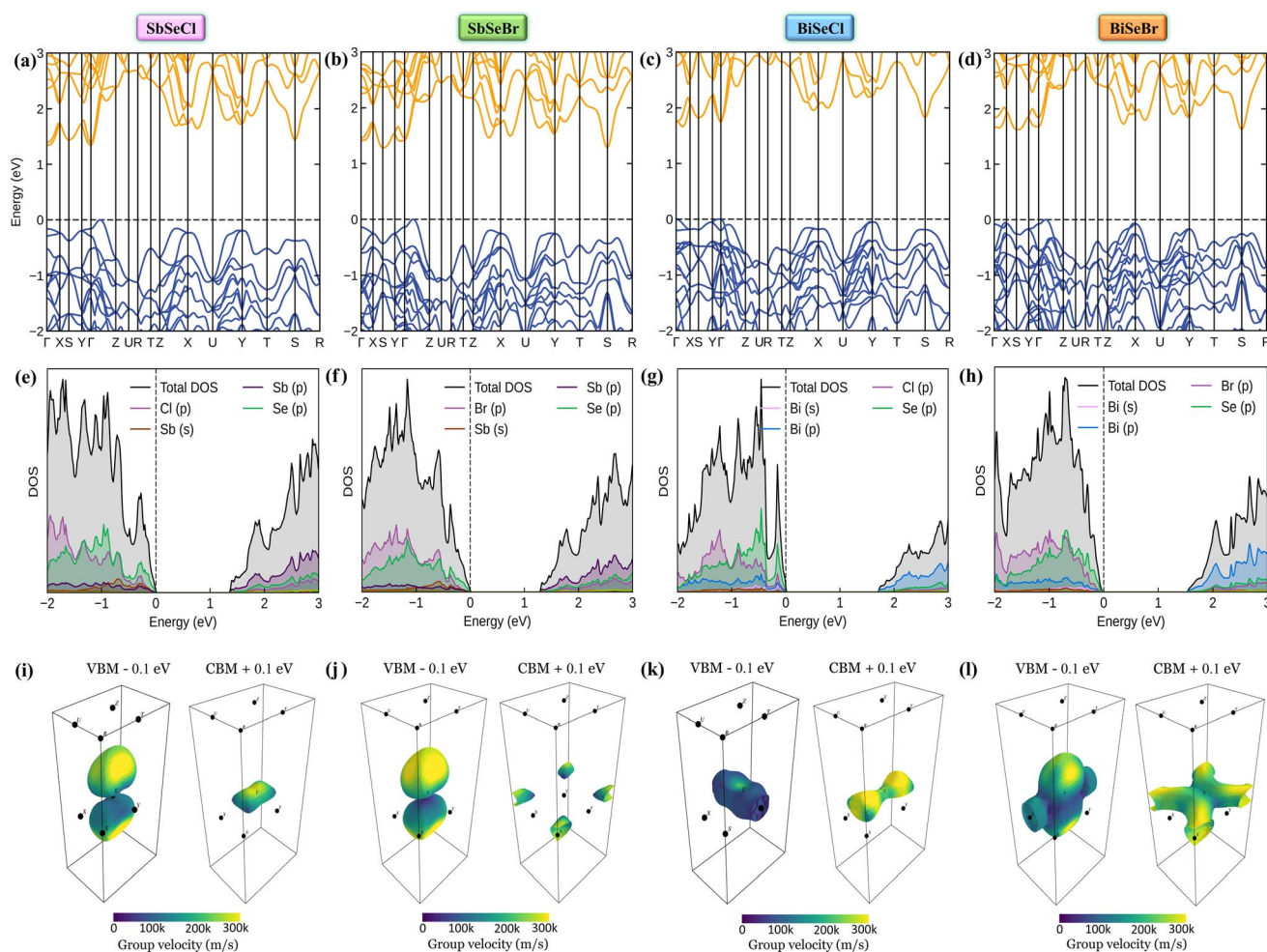

Fig. 3 (a−d) Electronic structure, (e−h) projected density of states and (i−l) Fermi surface near the VBM and CBM of SbSeCl, SbSeBr, BiSeCl, and BiSeBr, respectively. The left panel in Fig. (i−l) is for 0.1 eV below the VBM and the right panel is for 0.1 eV above the CBM, and the color represents their group velocity.

10698 | *J. Mater. Chem. A*, 2026, **14**, 10694–10707

This journal is © The Royal Society of Chemistry 2026

scattering between these modes. A detailed discussion on the implications of this feature in relation to phonon dispersion will be presented in Section 3.4.2.

The mechanical stability of the selenohalides was evaluated by computing their elastic constants, which were obtained using the stress–strain approach and are summarized in Table 2. In 2014, Mouhat *et al.* reformulated the Born stability criteria for all the crystal systems. For an orthorhombic lattice, the necessary and sufficient conditions are: $C_{11} > 0$, $C_{11}C_{22} > C_{12}^2$, $C_{11}C_{22}C_{33} + 2C_{12}C_{13}C_{23} - C_{11}C_{23}^2 - C_{22}C_{13}^2 - C_{33}C_{12}^2 > 0$, $C_{44} > 0$, $C_{55} > 0$, and $C_{66} > 0$.[51] All these six conditions are satisfied by the studied selenohalides, confirming their mechanical stability. Additional mechanical properties are provided in Section S1 and Table S2 of the SI. Notably, the Pugh's ratio (B/G) for all compounds exceeds the critical value of 1.75, indicating their ductile nature.[21] Furthermore, their Poisson's ratios lie in the range of 0.3–0.4, suggesting mixed bonding characteristics.[52]

3.3. Electronic structure and effective mass

Based on the calculation results, no significant changes in the band edges were observed while considering the hybrid exchange correlational functional (HSE06), except for an increase in the band gap (refer to Fig. S4). Hence, the electronic properties of the studied selenohalides are calculated using the PBE functional with van der Waals correction. Fig. 3 displays the calculated electronic band structures alongside the projected density of states (DOS) as well as the Fermi surfaces, to assess the electronic transport and optical characteristics. The VBM and CBM are located at Γ-Z and Γ for SbSeCl, Γ-Z and S for SbSeBr, Γ and Γ-X for BiSeCl, and Γ-Z and S–Y for BiSeBr, confirming the presence of indirect band gaps in all the investigated selenohalides (see Fig. 3(a–d)). The calculated band gap spans from 1.28 to 1.66 eV, which are well consistent with earlier reports (refer to Table 3). The sharp band edges result in smaller carrier effective masses rather than flat edges, resulting in high carrier mobility and electrical conductivity. As inferred from the projected DOS, shown in Fig. 3(e and h), the VBM of all the selenohalides is primarily contributed by the Se p-orbital while the CBM is dominated by the Sb/Bi p-orbital.

For further insights, the Fermi surface below and above 0.1 eV from the band edges is displayed in Fig. 3(i–l). The color scale represents the carrier group velocities. In SbSeCl, a complete hole pocket is observed, extending from Γ to Z, with

Table 3 Comparing the computed and reported band gaps of the studied selenohalides

Material	Band gap (eV)	Remarks
SbSeCl	1.34	This work
SbSeBr	1.28	This work
	1.18	Theo[53]
BiSeCl	1.66	This work
	1.69	Theo[54]
BiSeBr	1.63	This work
	1.54	Expt[44]

Table 4 Calculated effective mass of the carriers (in terms of m_0) along different crystallographic directions

Material	Γ-X		Γ-Y		Γ-Z	
	m_h^*	m_e^*	m_h^*	m_e^*	m_h^*	m_e^*
SbSeCl	2.41	1.24	3.39	0.62	0.95	0.29
SbSeBr	3.92	1.81	1.79	1.18	1.21	0.23
BiSeCl	1.69	0.65	2.43	0.35	0.44	0.17
BiSeBr	0.27	0.57	0.87	0.81	0.66	0.36

a corresponding downward dispersion arising from the symmetry of the Brillouin zone (BZ). Similarly, a pillow-shaped electron pocket is noted from Γ to X. In comparison, the Fermi surface of BiSeBr is widely spread over the entire BZ. Holes have the highest group velocity in antimony selenohalides, while in bismuth selenohalides it is electrons. Furthermore, the carrier effective masses along different crystallographic directions are calculated using the AMSET code (refer to Table 4).[39] The calculated carrier effective masses reveal a clear asymmetry between electrons (m_e^*) and holes (m_h^*), which has direct relationship to charge transport. Across all selenohalides and transport directions (Γ-X, Γ-Y, Γ-Z), holes are consistently heavier than electrons, except for BiSeBr (x-direction). For instance, in BiSeCl, m_h^* ranges from 1.69 to 2.43 m_0, whereas m_e^* varies only between 0.17 and 0.65 m_0. Here m_0 is the rest mass of the electron. This difference indicates that the mobility of electrons will be much higher than holes, favoring n-type conduction. In case of electrons, the favorable transport channels occur along Γ-Z direction for all the four selenohalides: 0.29 m_0 (SbSeCl), 0.23 m_0 (SbSeBr), 0.17 m_0 (BiSeCl), and 0.36 m_0 (BiSeBr). These values are significantly lower than those along the other directions, highlighting z-axis as the most favorable conduction pathway for electrons. In the case of holes, SbSeCl has heavy holes along Γ-X (2.41 m_0) and Γ-Y (3.39 m_0) than Γ-Z (0.95 m_0). In SbSeBr, largest hole mass of 3.92 m_0 is observed along Γ-X, while the smallest value of 1.21 m_0 along Γ-Z. These results suggest that z-direction not only favors n-type transport but also for p-type. Among the studied compounds, SbSeBr and BiSeCl are particularly essential. SbSeBr exhibits heavy hole effective mass (up to 3.92 m_0), indicating of limited hole mobility, while retaining relatively light electrons along Γ-Z (0.23 m_0), favoring efficient n-type conduction. On the other hand, BiSeCl displays the lowest electron effective mass within series (0.17 m_0 along Γ-Z) together with moderately heavy holes, suggesting an intrinsic preference for electron-dominated transport.

3.4. Thermoelectric properties

3.4.1. Electron transport properties. For all the selenohalides, the transport properties are calculated using advanced and efficient AMSET program for both carrier types at 300 K and 600 K.[39] One of the members in this family, BiSeI, is found to exhibit n-type transport, with electrons as the majority carriers. With this note, n-type transport properties are presented in Fig. 4, while the p-type properties are provided in Fig. S5 for reference. The discussions of transport properties are based on
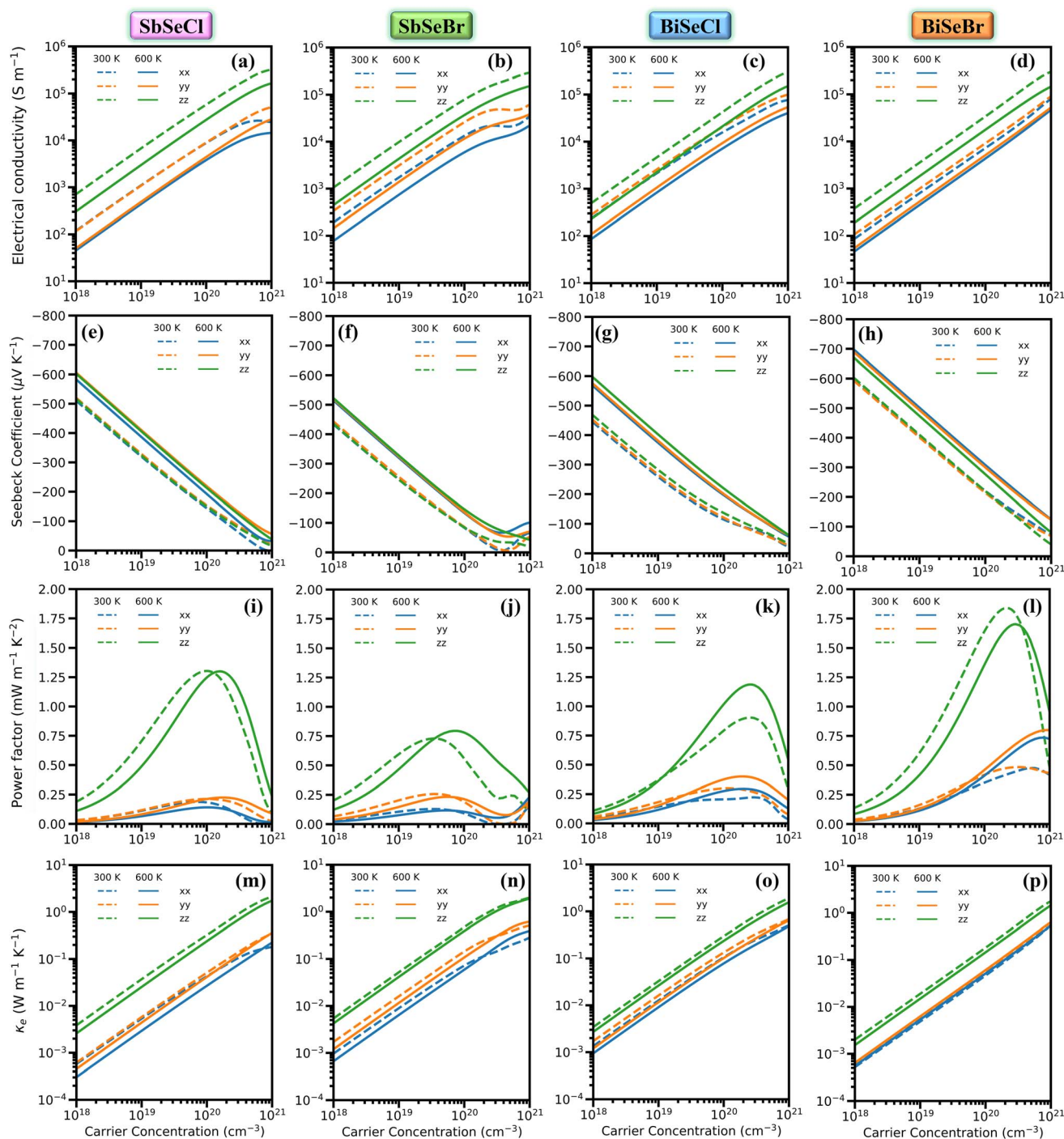
This journal is © The Royal Society of Chemistry 2026

J. Mater. Chem. A, 2026, **14**, 10694–10707 | **10699**

Fig. 4 (a–d) Electrical conductivity, (e–h) Seebeck coefficient, (i–l) power factor and (m–p) electronic thermal conductivity of *n*-type SbSeCl, SbSeBr, BiSeCl, and BiSeBr. The dotted and solid lines indicate 300 and 600 K, respectively, while the color variation represents different crystallographic directions.

a fixed carrier concentration of $n = 1 \times 10^{20}\ cm^{-3}$. The n-type and p-type electrical conductivity as a function of carrier concentration is illustrated in Fig. 4(a–d) and S5(a–d). Irrespective of materials and carrier types, σ increases with respect to n, satisfying the relation $\sigma = ne\mu$. Here, μ is the mobility of the carrier and n is the corresponding charge. Apart from SbSeBr, all the selenohalides exhibit almost similar magnitude of σ along *x*- and *y*-direction, while significant anisotropy is

observed along *z*-direction. For all cases, σ is highest along *z*-direction, owing to the larger structural spacing provided by chemical bonding compared to the van der Waals interactions governing other directions. For *n*-type systems, across all crystallographic directions, σ is generally one to two orders higher than their counterparts, which can be directly attributed to the smaller effective masses of electron than holes (refer to Table 4). For instance, in BiSeCl, m_e^* varies between 0.17 and 0.65 m_0,

10700 | *J. Mater. Chem. A*, 2026, **14**, 10694–10707

This journal is © The Royal Society of Chemistry 2026

while m_h^* lies between 1.69 and 2.43 m_0. The lighter electrons can move faster, and thus higher n-type electrical conductivity is observed. For example, along the z-direction, $\sigma = 42\,244$ S m^{-1} at 300 K for n-type, while p-type has only 4772 S m^{-1}. Furthermore, the anisotropy in σ mirrors the trend observed in directional effective mass. For example, in SbSeBr, the m_e^* is lowest along Γ-Z ($m_e^* = 0.23\ m_0$), which corresponds to the highest conductivity along the z-direction at 300 K (78\,757 S m^{-1}). Similarly, SbSeCl exhibits moderate m_e^* values (0.29–1.24 m_0), resulting in intermediate conductivity values ranging from 8826 to 57\,910 S m^{-1}. Interestingly, temperature has a pronounced effect on conductivity, with all compounds showing a substantial decrease in σ, when heated from 300 to 600 K. This reduction can be attributed to enhanced carrier scattering, which restricts the mobility of the carrier. For instance, the n-type conductivity of BiSeCl drops from 42\,244 S m^{-1} (300 K, z-direction) to 21\,064 S m^{-1} (600 K, z-direction). A similar trend is also evident in p-type materials, where the σ of SbSeCl decreases from 11\,137 S m^{-1} at 300 K to 4670 S m^{-1} at 600 K, along the z-direction. Overall, SbSeBr and BiSeCl show high σ, consistent with their relatively small m_e^* along specific transport directions. The σ values for all selenohalides are given in the table for clarity (refer to Table S3 and S4). SbSeCl shows moderate performance, while the conductivity of BiSeBr is affected by its larger carrier effective masses. The correlation between directional effective mass and anisotropic conductivity highlights the critical role of band structure engineering in optimizing the thermoelectric performance.

The calculated Seebeck coefficient as a function of carrier concentration is displayed in Fig. 4(e–h). For n-type BiSeBr, along the x-direction, at $T = 300$ K and $n = 1 \times 10^{20}$ cm^{-3}, the S value ranges from −83 to −220 μV K^{-1}, while at 600 K, the magnitude increases significantly, reaching as high as −308 μV K^{-1}. This trend confirms that the thermal excitation of the carriers affects the S of the n-type system. Among the selenohalides, BiSeBr exhibits the largest negative S value, suggesting superior thermoelectric potential upon n-type doping, while SbSeCl and SbSeBr show relatively lower magnitudes (refer to Table S5 and S6). For the p-type case, at 300 K, the S values lie between 147 and 298 μV K^{-1}, while at 600 K, they increase markedly to 227–386 μV K^{-1}. Notably, p-type BiSeCl exhibits the highest S value at 300 K (~298 μV K^{-1} along the y-direction), which exceeds 370 μV K^{-1} (along the y- and z-directions) at 600 K. The observed temperature dependence of S aligns well with the general behavior of semiconductors, where thermal excitation broadens the carrier distribution and alters the conductivity. Anisotropy effects are considerable, suggesting direction-dependent electron transport properties, which are common in layered materials.

To examine the coupling effect of S and σ, the power factor is calculated as a function of carrier concentration and displayed in Fig. 4(i–l). It reveals clear distinctions between n- and p-type doping accompanied by strong anisotropy across crystallographic directions. In Bi-based systems, n-type systems consistently exhibit higher PF than their counterparts, both at 300 and 600 K, highlighting the superior role of lighter electrons in facilitating higher electrical transport. At 300 K, for n-type

doping, the highest PF occurs predominantly along the z-direction, with SbSeCl, SbSeBr, BiSeCl, and BiSeBr reaching 1.30, 0.56, 0.79 and 1.64 mW m^{-1} K^{-2}, respectively. This noticeable PF along the z-direction can be related to the interplay between the intermediate electron effective mass and favorable transport along the chain direction. In contrast, PF along the x- and y-directions remains below 0.42 mW m^{-1} K^{-2}, underscoring the highly anisotropic nature of charge transport. At elevated temperature (600 K), the PF of n-type systems increases, except for SbSeCl and BiSeBr (z-direction), but the directional trends are retained. For example, the z-direction remains the most favorable in SbSeCl (1.27 mW m^{-1} K^{-2}), SbSeBr (0.78 mW m^{-1} K^{-2}), BiSeCl (1.01 mW m^{-1} K^{-2}), and BiSeBr (1.35 mW m^{-1} K^{-2}). In contrast, the p-type systems display significantly smaller PF values along all directions and temperatures. At 300 K, the maximum p-type PF is observed for SbSeBr along the y-direction (0.55 mW m^{-1} K^{-2}), while other compounds exhibit considerably lower values, typically below 0.38 mW m^{-1} K^{-2}. Increasing the temperature to 600 K, alters the PF further, with most values falling in the range of 0.06 to 0.45 mW m^{-1} K^{-2}. The comparatively lower performance in p-type systems can be directly linked to the heavier hole effective mass, which suppresses the mobility and limits the electrical conductivity. Refer to Tables S7 and S8 for better comparison.

The calculated κ_e as a function of carrier concentration is shown in Fig. 4(m–p). The obtained κ_e reveals significant temperature dependence, carrier-type dependence, and notable directional anisotropy. Across all selenohalides and directions, κ_e decreases considerably as temperature increases. This behavior is ascribed to the enhanced phonon–electron scattering at higher temperatures, thereby reducing the contribution of charge carriers to thermal transport. In n-type SbSeBr (y-direction), κ_e drops from 0.144 W m^{-1} K^{-1} at 300 K to 0.108 W m^{-1} K^{-1} at 600 K (~25% reduction). Similarly, in p-type SbSeBr (y-direction), κ_e decreases from 0.136 W m^{-1} K^{-1} to 0.066 W m^{-1} K^{-1} (~51% reduction). A strong directional dependence of κ_e is observed in most compounds, particularly for n-type doping. For n-type BiSeCl at 300 K, κ_e along the z-direction is 0.298 W m^{-1} K^{-1}, which is ~2.8 times higher than that along the x-direction i.e., 0.105 W m^{-1} K^{-1}. Similarly, for p-type SbSeCl, at 300 K, κ_e is 0.069 W m^{-1} K^{-1} along the y-direction, while κ_e is 0.023 W m^{-1} K^{-1} along the x-direction, showing strong anisotropy. For the studied compounds, n-type systems exhibit significantly higher κ_e compared to their counterparts, especially along the z-direction, associated with the behavior of σ. In n-type SbSeBr, at 300 K, along the z-direction, the observed κ_e is 0.473 W m^{-1} K^{-1}, which is nearly seven times higher than in p-type i.e., 0.066 W m^{-1} K^{-1}. This trend is consistent at 600 K, although the absolute values tend to decrease. The higher electronic thermal conductivity in n-type materials indicates that electrons have better mobility than holes, likely originating from conduction-band curvature differences and lower effective masses of electrons. The κ_e values for all selenohalides are listed in Table S9 and S10.

3.4.2. Phonon transport properties. The lattice thermal conductivity is calculated using the ShengBTE program and is illustrated in Fig. 5(a–d).[37] The κ_L for the studied selenohalides

This journal is © The Royal Society of Chemistry 2026

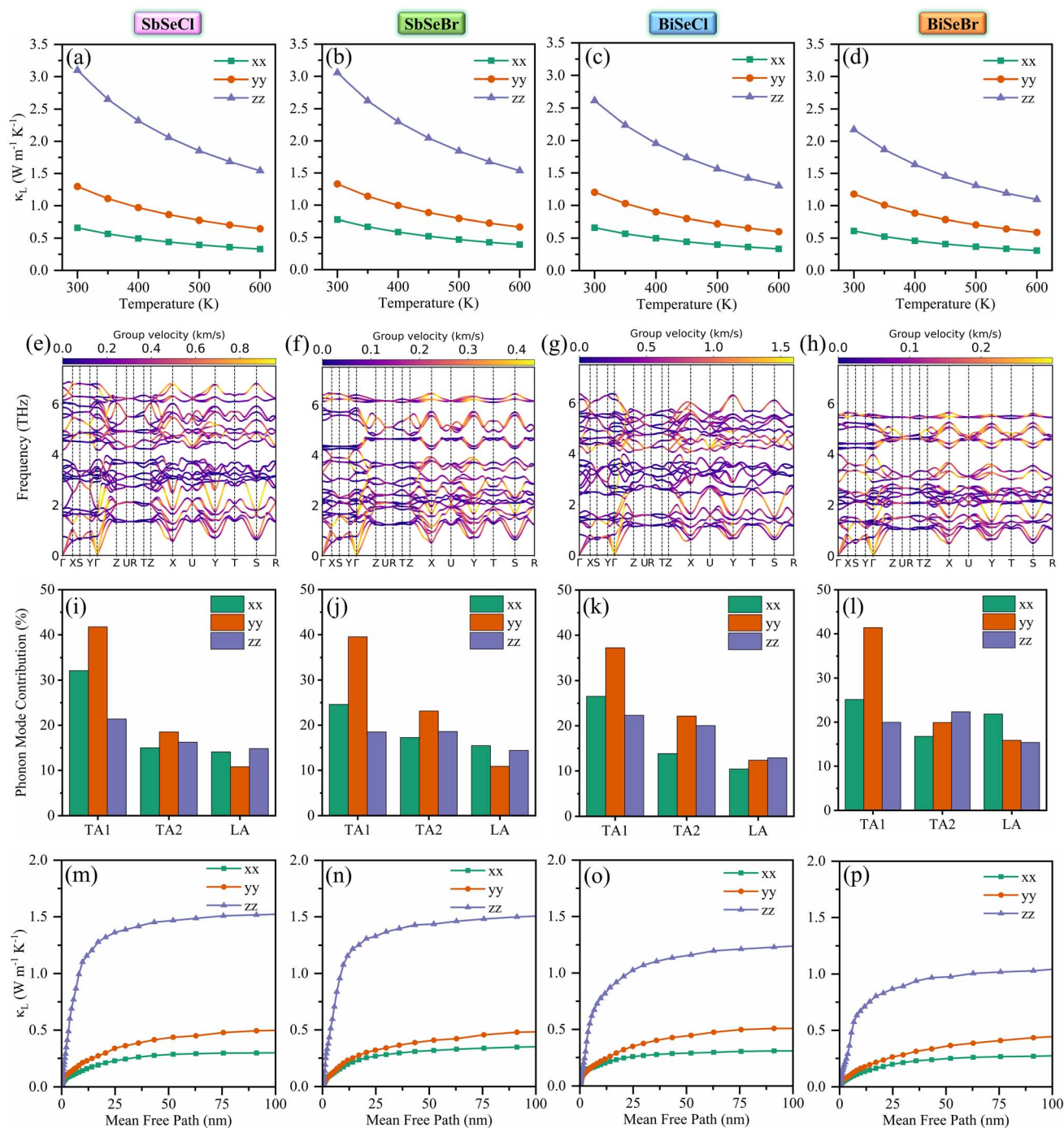J. Mater. Chem. A, 2026, **14**, 10694–10707 | **10701**

Fig. 5 (a–d) Temperature dependent lattice thermal conductivity, (e–h) group velocity projected phonon dispersion, (i–l) percentage of acoustic mode contribution to κ_L (m–p) κ_L as a function of mean free path at 600 K for SbSeCl, SbSeBr, BiSeCl, and BiSeBr along different directions. The color spectrum in (e–h) indicates the magnitude of group velocity.

along the three directions decreases with temperature. For all selenohalides, the direction trend of κ_L increases from the x- to z-direction. For example, in SbSeCl, at 300 K, κ_L along the x-, y-, and z-directions is 0.66, 1.30 and 3.10 W m^{-1} K^{-1}, respectively. With an increase in temperature to 600 K, κ_L decreases by roughly half $i.e.$, 0.33, 0.64 and 1.54 W m^{-1} K^{-1}, owing to the inverse relationship with T and the enhanced phonon scattering process. Similar to the trend in highest frequencies in

phonon dispersion, κ_L decreases from SbSeCl to BiSeBr, ascribed to the inherent relationship between phonon frequency and κ_L. Compared to all the selenohalides, BiSeBr results in low thermal conductivity due to presence of heavier Bi and Br elements. To understand further, the group velocity and Grüneisen parameter were projected above the phonon dispersion, as shown in Fig. 5(e–h) and S6(a–d). As expected, v_g of acoustic modes is higher than that of optical modes, and it

10702 | J. Mater. Chem. A, 2026, 14, 10694–10707

This journal is © The Royal Society of Chemistry 2026

decreases with the change in halogen elements, ascribed to the larger vibration of heavier atoms, which resists the phonon transport. For example, the range of v_g for SbSeCl is from 0.0 to 0.95 km s^{-1}. By introducing Br into the lattice, it decreases nearly twofold i.e., 0.0–0.45 km s^{-1}. In addition, lower (larger) v_g is observed along the x-direction (z-direction), visualized from the acoustic modes. Generally, the crystal with strong anharmonicity exhibits lower phonon transport and the Grüneisen parameter is the metric to quantify it. Irrespective of selenohalides, the Grüneisen parameter of the acoustic modes along the x-direction is larger than along other directions, indicating stronger anharmonicity. The combination of small group velocity and large Grüneisen parameter results in ultra-low lattice thermal transport along the x-direction.

To uncover the origin of κ_L further, the individual phonon mode contribution to κ_L is computed. For all the selenohalides, along all the directions, the percentage of acoustic mode contribution to κ_L is illustrated in Fig. 5(i–l) and that for optical modes is shown in Fig. S7. As expected, irrespective of the systems and directions, the acoustic modes show dominant contribution to κ_L, ascribed to the higher phonon group velocities. For example, the three acoustic modes collectively contribute almost 60% of κ_L in the case of SbSeCl at 300 K along the x-direction. It is worth noting that the influence of the TA1 mode to κ_L along the y-direction is much higher than in the considered cases. In addition, the TA1 mode exhibits the strongest anisotropy, for example, in SbSeCl, significant differences are observed along each direction, i.e., 31% along x, 41% along y and 21% along z, highlighting the crucial role of

transverse vibrations. Low-frequency optical mode e.g., O1 show appreciable contributions ($\approx$9–3% each), reflecting their coupling with the acoustic modes and indicating their importance in the phonon–phonon scattering process. Mid-frequency optical modes like O6 and O7 modes yield larger portion of κ_L along the z-direction. The contributions from other modes are not appreciable, except for O10 (6.9%), O11 (6.5%) and O17 (5.4%) of BiSeCl along the x-direction. These results suggest that the absolute magnitudes of mode contributions vary slightly between the materials, but the overall vibrational anisotropy and mode dependence remain remarkably similar. In each case, acoustic modes dominate heat-carrying capacity, whereas optical modes provide scattering channels that limit phonon transport. This consistent trend indicates a common underlying mechanism controlling their lattice dynamics, implying that the difference in lattice thermal conductivity among these compounds is primarily governed by secondary factors like mass contrast, bonding strength, and anharmonicity.

To demonstrate the effect of nanostructuring on κ_L, the cumulative lattice thermal conductivity (κ_{cum}) as a function of phonon mean free path (MFP) at 600 K was calculated. As depicted in Fig. 5(m–p), phonon transport is dominated along the z-direction, due to the presence of chains. For all the four systems, the majority of κ_L is accumulated below 50 nm MFPs, indicating that the phonon transport is largely governed by short- to intermediate-range phonons. Interestingly, κ_L along the z-axis reaches its maximum contribution within a short
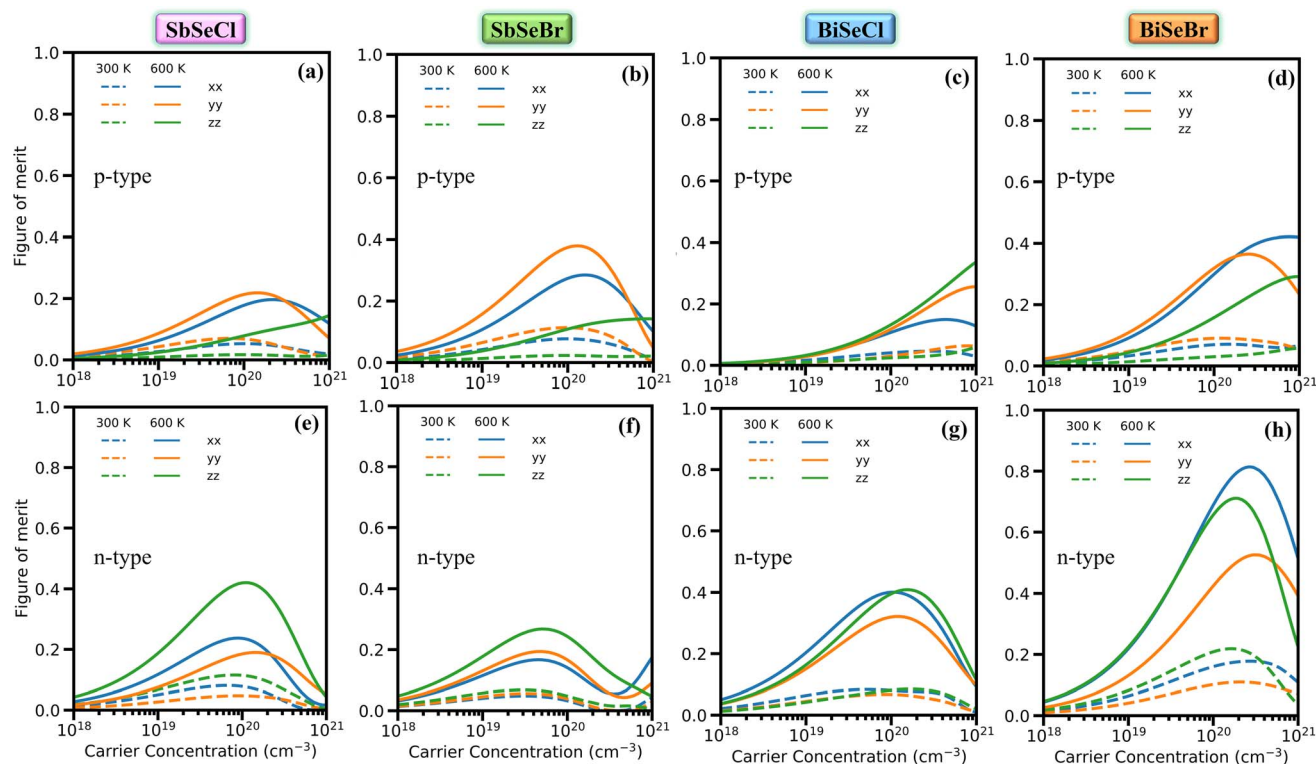

Fig. 6 The calculated carrier dependent zT for (a–d) p-type and (e–h) n-type SbSeCl, SbSeBr, BiSeCl and BiSeBr. The dotted and solid lines correspond to 300 and 600 K and the color variation represents different crystallographic directions.

This journal is © The Royal Society of Chemistry 2026

J. Mater. Chem. A, 2026, **14**, 10694–10707 | **10703**

range, indicating the need for fine-nanostructuring to utilize the systems at their maximum potential.

3.4.3. Figure of merit. The TE performance of the studied selenohalides is evaluated through zT at different temperatures (300 and 600 K) for both n- and p-type doping (refer to Fig. 6). Due to the anisotropic nature of transport properties, the calculated zT also reveals significant variations among the four selenohalides along different crystallographic directions. Overall, zT increases with temperature, showing that these selenohalides exhibit better efficiency at high-temperature regimes. For example, n-type SbSeCl along the z-direction shows an increase from 0.11 at 300 K to 0.42 at 600 K, corresponding to an almost fourfold improvement. Similarly, p-type SbSeBr exhibits a rise from 0.11 to 0.38 over the same temperature range, along the y-direction. This improvement can be attributed to the increased Seebeck coefficient and the reduction of lattice thermal conductivity at higher temperatures, owing to the secondary band contribution and enhanced phonon scattering, respectively. A comparative analysis of n-type and p-type doping shows that, in most cases, n-type doping leads to higher zT values (refer to Table S11). At 600 K, the overall highest performance is obtained for n-type BiSeBr along x-direction, where a zT value of 0.81 is attained at $n = 3.0 \times 10^{20}$ cm^{-3}, which is nearly double the performance of its p-type counterpart in the same direction ($zT = 0.42$). This superior n-type behavior in these compounds is primarily due to higher electron mobility and smaller effective masses. However, certain p-type systems also exhibit competitive performance, such as p-type SbSeBr along the y-direction, achieving a relatively high zT of ∼0.38 at 600 K. These findings suggest that both carrier types can be optimized, depending on the material and desired operating temperature. The obtained zT is comparable with experimentally reported chalcohalide family and halogen-doped candidates such as $Bi_{13}S_{18}Br_2$ (1.0 at 748 K) and $PbSnS_{1.96}Br_{0.04}$ (0.82 at 873 K).[55,56] Overall, these results suggest that n-type BiSeBr can be a potential candidate for high-temperature thermoelectric devices, while SbSeBr may be suitable for p-type applications.

3.5. Photovoltaic properties

3.5.1. Dielectric properties. As observed, the band gaps of the investigated selenohalides fall within the range of 1.28 to 1.66 eV, making them promising candidates for photovoltaic applications. The calculated optical properties are strongly correlated with their dielectric properties. The real part of the dielectric function, shown in Fig. 7(a), represents the degree of polarizability of the selenohalides. At zero photon energy, the static dielectric constants Re(ε) are found to be approximately 10.22 (SbSeCl), 11.63 (SbSeBr), 9.77 (BiSeCl), and 11.03 (BiSeBr), indicating relatively strong dielectric screening. Such moderately high Re(ε) values are desirable for photovoltaic absorbers as they effectively reduce the coulombic binding between photogenerated electron–hole pairs, thereby promoting efficient charge separation. A sharp increase in Re(ε) is observed around 1.5–3.0 eV, which corresponds to the onset of significant optical transitions from the valence band to the conduction
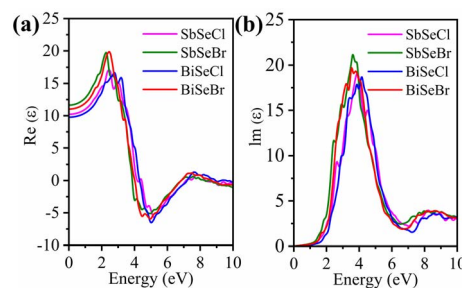

Fig. 7 The calculated energy dependent (a) real and (b) imaginary part of the dielectric function.

band. BiSeBr exhibits the highest peak value of 19.9, followed closely by SbSeBr and SbSeCl, while BiSeCl shows a slightly lower maximum. The dominance of Br-based compounds can be attributed to their enhanced electronic polarizability, arising from their larger ionic radius.

The imaginary part, shown in Fig. 7(b), is directly related to the optical absorption coefficient and provides information about the inter-band electronic transitions. All compounds exhibit a sharp absorption onset near 1.5 eV, which aligns with their semiconducting band gaps, confirming their effective capability to absorb visible light. The highest peaks are observed for SbSeBr (Im(ε) = 21.1) and BiSeBr (19.6) followed by SbSeCl (19) and BiSeCl (18.7) suggesting the strong absorption in Br-based compounds. The stronger optical transitions in Br-containing compounds can be attributed to the reduced band dispersion, leading to increased oscillator strength. Multiple peaks between 3.0 and 5.0 eV indicate the presence of complex inter-band transitions. The broader response around 8–9 eV suggests the potential of these materials to harvest photons across a wide spectral range, making them promising for both visible-light photovoltaics and optoelectronic devices.

3.5.2. Excitonic properties. The exciton binding energy (E_b) measures the stability of electron–hole pairs. For efficient solar cells, a lower E_b value is desirable, since electrons can easily dissociate at room temperature. The E_b is calculated using the Wannier–Mott formula, $E_b = 1/2\varepsilon_s a_0$. Here, ε_s is the static dielectric constant and a_0 is the Wannier–Mott exciton radius given by $a_0 = \varepsilon_s/\mu$. Here, the reduced effective mass (μ) is obtained as $\mu = m_e m_h/m_e + m_h$.[57,58] The effective mass of the carriers is obtained from the band edges using the AMSET code. The calculated excitonic properties are shown in Table 5. Irrespective of the materials, the electrons are lighter than holes. These smaller effective masses can also lead to strong inter-band transitions resulting in higher peaks in Im(ε), which are directly related to high absorption. Furthermore, static dielectric constants control the electrostatic screening and influence

Table 5 The calculated excitonic properties of the selenohalides

Material	$m_e^*(m_0)$	$m_h^*(m_0)$	ε_s	a_0 (Å)	E_b (meV)
SbSeCl	0.89	1.49	32.14	30.43	7.34
SbSeBr	0.89	1.21	24.88	25.64	11.28
BiSeCl	0.65	2.43	20.77	21.45	16.15
BiSeBr	0.69	1.01	19.70	25.53	14.30

10704 | *J. Mater. Chem. A*, 2026, **14**, 10694–10707

This journal is © The Royal Society of Chemistry 2026

the exciton formation. The larger ε_s noted for SbSeCl reflects its strong screening and weak exciton binding capacity. In contrast, lower values are observed for BiSeCl and BiSeBr, indicating the reduced screening potential. Among them, SbSeBr exhibits an intermediate ε_s value indicating a balanced trade-off between optical absorption and charge separation. The nearly similar optimal exciton Bohr radius observed for BiSeBr and SbSeBr results in efficient exciton separation. BiSeCl exhibits the highest E_b among the studied systems, representing the higher stability of excitons that can lead to reduced efficiency.[59] Thus far, SbSeBr is anticipated to exhibit favorable absorption characteristics, arising from its strong optical transitions, moderate exciton binding, and well-balanced charge transport. However, the calculated E_b values for the studied selenohalides are significantly lower than those of the benchmark photovoltaic candidates such as MAPbI$_3$ (45 meV) and Si (20 meV).[60] This indicates relatively weak exciton binding, which is advantageous for efficient charge separation and highlights the promise of these materials for photovoltaic applications.

3.5.3. Optical properties and photovoltaic efficiency. To explore their optical transition characteristics, the dipole–dipole transition probability (P^2) between the upper valence band (VB) and lower conduction band (CB) for SbSeCl, SbSeBr, BiSeCl, and BiSeBr is calculated (see Fig. 8(a–d)). A non-zero P^2 value indicates an allowed dipole transition between the VB and CB states. The intensity and distribution of these transitions depend on the symmetry and orbital character of the wavefunctions at each k-point. For example, SbSeCl exhibits strong transitions near the X and U points, suggesting the higher optical transition probability and enhanced light absorption at these sites (see Fig. 8(a)). Similarly, enhanced transitions are

observed at Y and U for SbSeBr; Z–X, X and U for BiSeCl; and U and Y for BiSeBr. In contrast, regions with zero or near-zero P^2 values along high-symmetry paths indicate dipole-forbidden or weakly allowed transitions, which correspond to reduced optical activity. Comparatively, the selenohalides with Br halogen have lager P^2 values than the Cl-based systems.

The optical absorption coefficient is a critical parameter in evaluating the light-harvesting potential of solar absorbers. To this end, the optical absorption spectra are derived from the frequency-dependent dielectric function for all the selenohalides, as shown in Fig. 8(e). Generally, a sharp increase in absorption is observed when the incident photon energy approaches the E_g of the material, a key feature of an efficient photovoltaic material. A pronounced exponential rise in absorption is evident near their respective band edges, consistent with the calculated E_g values. This behaviour is closely linked with the joint density of states (JDOS), where flatter band edges lead to a steeper rise in JDOS, near the band gap, thereby enhancing the absorption (Fig. 8(f)). Hence, the absorption trends are strongly correlated with the JDOS profile. Interestingly, selenohalides with Br halogen have higher absorption than Cl-based compounds, which can be associated with the behaviour of P^2.

To assess the photovoltaic potential of the selenohalides, spectroscopic limited maximum efficiency (SLME) calculations as a function of film thickness are performed and depicted in Fig. 8(g). This SLME approach accounts for various energetic sequences (dipole forbidden, dipole allowed and indirect E_g), photon absorptivity, and dependence of radiative recombination losses. This also facilitates the understanding of photovoltaic efficiency as a function of absorption layer thickness. However, a major limitation of this method is the exclusion of
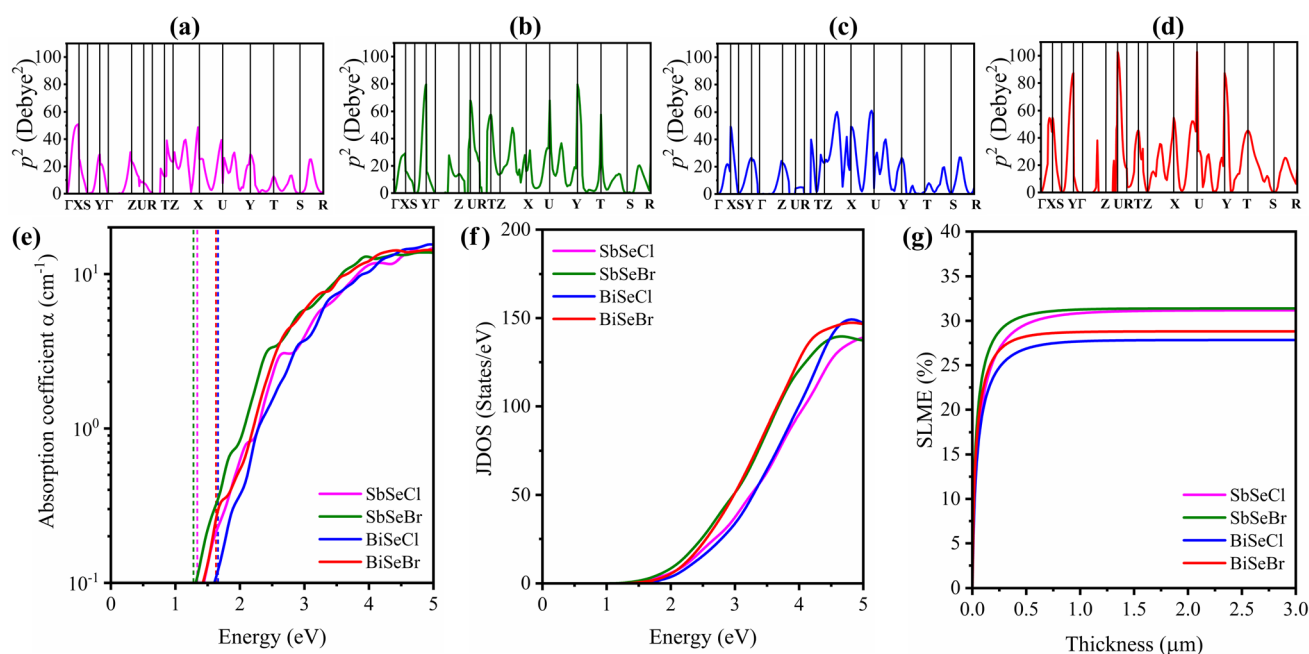

Fig. 8 The dipole−dipole transition probability along different k-points for (a) SbSeCl, (b) SbSeBr, (c) BiSeCl and (d) BiSeBr. (e) Optical absorption, (f) joint density of states and (g) spectroscopic limited maximum efficiency. The dotted line in (e) represents the fundamental gap.

This journal is © The Royal Society of Chemistry 2026

J. Mater. Chem. A, 2026, **14**, 10694–10707 | **10705**

non-radiative recombination, which significantly limits the efficiency of most of the indirect band gap absorbers. In these calculations, the dielectric response computed using the PBE + D3 functional. For all the compounds, SLME increases rapidly with thickness and saturates thereafter. Notably, under 1-sun illumination AM1.5 G, the Sb-based selenohalides achieve higher SLME values up to ~31% at a thickness of 0.5 μm, while Bi-based compounds yield slightly lower efficiencies, around 27% at the same thickness, within the radiative limit. This performance difference can be attributed to the stronger optical transition intensities and absorption features observed in Sb-based systems. However the calculated SLME values are larger than those of the established candidates such as Si (26.1%) and $CuInSe_2$ (~23%).[61,62]

4. Conclusions

This work systematically explored the thermoelectric and photovoltaic potential of quasi-1D selenohalides using first-principles calculations. The weak van der Waals interlayer interactions combined with heterogeneous intralayer bonding give rise to distinct electron and phonon transport characteristics. Stability was confirmed through formation energy, convex hull analysis, phonon spectra, and elastic constants, while chemical potential diagrams suggest their synthesizability. The calculated band gaps (1.28–1.66 eV) and favorable carrier effective masses underscore their suitability for energy applications. From a thermoelectric perspective, n-type transport dominates, with attractive electron transport characteristics along the z-direction, facilitated by extended bonding pathways. Despite mixed bonding characteristics, lattice thermal conductivity remains below 2 W m^{-1} K^{-1} at 600 K. Notably, n-type BiSeBr exhibits the best performance, achieving a zT of 0.81 at 600 K along the z-direction, driven by its high-power factor (1.36 W m^{-1} K^{-1}) and moderate lattice thermal conductivity (1.09 W m^{-1} K^{-1}). On the photovoltaic side, SbSeBr demonstrates small effective masses, moderate exciton binding energies, and strong optical absorption, leading to a spectroscopic limited maximum efficiency of ~31% at a film thickness of 0.5 μm under 1-sun illumination AM1.5 G. Overall, quasi-1D selenohalides emerge as promising candidates for thermoelectric and photovoltaic applications, warranting further experimental validation.

Author contributions

Prakash Govindaraj: conceptualization, software, formal analysis, investigation, writing – original draft, writing – review & editing, visualization, data curation, validation, methodology. Hern Kim: supervision, resources, project administration, data curation, funding acquisition, conceptualization.

Conflicts of interest

The authors declare no conflict of interest.

Data availability

The computational results that predominantly support our claims were calculated using the Vienna *Ab Initio* Simulation Package (VASP) and can be found at https://www.vasp.at/ with https://doi.org/10.1103/PhysRevB.54.11169 and https://doi.org/10.1103/PhysRevB.59.1758. The version of the code employed for this study is version 5.4.

Supplementary information (SI): the convergence test of q-point, cut-off radius and interpolation factor to calculate phonon and electron transport properties; 3D ELF, bond length and mechanical properties; validating the suitability of exchange correlational functional; electron transport properties of hole doped selenohalides; Gruneisen projected phonon dispersion; phonon mode contribution to KL, and peak zT along different directions. See DOI: https://doi.org/10.1039/d5ta08032k.

Acknowledgements

References

1 T. Kirchartz, G. Yan, Y. Yuan, B. K. Patel, D. Cahen and P. K. Nayak, *Nat. Rev. Mater.*, 2025, 1–20.

2 X.-L. Shi, N.-H. Li, M. Li and Z.-G. Chen, *Chem. Rev.*, 2025, **16**, 7525–7724.

3 G. J. Snyder and E. S. Toberer, *Nat. Mater.*, 2008, **7**, 105–114.

4 H. He, J. Song, R. Liang, G. Yan, Y. Geng, L. Hu, F. Liu, W. Ao and C. Zhang, *Small*, 2025, **21**, 2408864.

5 F. Xu, B. Liu and R. Ang, *Acta Mater.*, 2025, 121266.

6 K. Imasato, S. Fujimoto, Y. Ikuta, M. Miyata, N. Saitoh, N. Yoshizawa, A. Yamamoto, T. Ishida, M. Koyano and M. Ohta, *ACS Appl. Mater. Interfaces*, 2025, **17**, 25478–25488.

7 H. Ming, Z.-Z. Luo, Z. Zou and M. G. Kanatzidis, *Chem. Rev.*, 2025, **125**, 3932–3975.

8 T. Deng, P. Qiu, T. Yin, Z. Li, J. Yang, T. Wei and X. Shi, *Adv. Mater.*, 2024, **36**, 2311278.

9 D. Singh and R. Ahuja, *Wiley Interdiscip. Rev.: Comput. Mol. Sci.*, 2022, **12**, e1547.

10 H. Han, L. Zhao, X. Wu, B. Zuo, S. Bian, T. Li, X. Liu, Y. Jiang, C. Chen and J. Bi, *J. Mater. Chem. A*, 2024, **12**, 24041–24083.

11 C. Wu, X.-L. Shi, L. Wang, W. Lyu, P. Yuan, L. Cheng, Z.-G. Chen and X. Yao, *ACS Nano*, 2024, **18**, 31660–31712.

12 X. Han, Y. Ji and Y. Yang, *Adv. Funct. Mater.*, 2022, **32**, 2109625.

13 B. Anand, R. Shankar, S. Murugavelh, W. Rivera, K. M. Prasad and R. Nagarajan, *Renewable Sustainable Energy Rev.*, 2021, **141**, 110787.

14 H. Zhang, Y. Xia, Y. Zhang, U. V. Ghorpade, M. He, S. W. Shin, X. Hao and M. P. Suryawanshi, *Advanced Science*, 2025, **12**, 2413131.

15 S. Luo, T. Li, X. Wang, M. Faizan and L. Zhang, *Wiley Interdiscip. Rev.: Comput. Mol. Sci.*, 2021, **11**, e1489.

10706 | *J. Mater. Chem. A*, 2026, **14**, 10694–10707

This journal is © The Royal Society of Chemistry 2026

16 B. Kozinsky and D. J. Singh, *Annu. Rev. Mater. Res.*, 2021, **51**, 565–590.

17 J. Li, S. S. Han and S. P. Guo, *Eur. J. Inorg. Chem.*, 2022, **2022**, e202200419.

18 S. Shyamal and N. Pradhan, *ACS Energy Lett.*, 2023, **8**, 3902–3926.

19 X. H. Li, Z. H. Shi, M. Yang, W. Liu and S. P. Guo, *Angew. Chem.*, 2022, **134**, e202115871.

20 B. Peng, K. Xu, H. Zhang, Z. Ning, H. Shao, G. Ni, J. Li, Y. Zhu, H. Zhu and C. M. Soukoulis, *Adv. Theory Simul.*, 2018, **1**, 1700005.

21 P. Govindaraj and K. Venugopal, *J. Alloys Compd.*, 2022, **929**, 167347.

22 D. Tiwari, F. Cardoso-Delgado, D. Alibhai, M. Mombrú and D. J. Fermín, *ACS Appl. Energy Mater.*, 2019, **2**, 3878–3885.

23 V. Donges, *Z. Anorg. Allg. Chem.*, 1950, **263**, 280–291.

24 P. Chauhan, J. Singh and A. Kumar, *J. Mater. Chem. A*, 2024, **12**, 16129–16142.

25 A. Bafekry, M. Faraji, M. Fadlallah, D. Hoat, H. Jappor, I. A. Sarsari, M. Ghergherehchi and S. Feghhi, *Phys. Chem. Chem. Phys.*, 2021, **23**, 25866–25876.

26 G. Kresse and J. Furthmüller, *Phys. Rev. B*, 1996, **54**, 11169.

27 G. Kresse and D. Joubert, *Phys. Rev. B*, 1999, **59**, 1758.

28 J. P. Perdew, K. Burke and M. Ernzerhof, *Phys. Rev. Lett.*, 1996, **77**, 3865.

29 S. Grimme, S. Ehrlich and L. Goerigk, *J. Comput. Chem.*, 2011, **32**, 1456–1465.

30 H. J. Monkhorst and J. D. Pack, *Phys. Rev. B*, 1976, **13**, 5188.

31 K. Momma and F. Izumi, *Appl. Crystallogr.*, 2011, **44**, 1272–1276.

32 A. M. Ganose, A. J. Jackson and D. O. Scanlon, *J. Open Source Softw.*, 2018, **3**, 717.

33 R. Nelson, C. Ertural, J. George, V. L. Deringer, G. Hautier and R. Dronskowski, *J. Comput. Chem.*, 2020, **41**, 1931–1940.

34 Y. Kumagai, N. Tsunoda, A. Takahashi and F. Oba, *Phys. Rev. Mater.*, 2021, **5**, 123803.

35 A. Togo, L. Chaput, T. Tadano and I. Tanaka, *J. Phys.: Condens. Matter*, 2023, **35**, 353001.

36 A. Togo, *J. Phys. Soc. Jpn.*, 2023, **92**, 012001.

37 W. Li, J. Carrete, N. A. Katcho and N. Mingo, *Comput. Phys. Commun.*, 2014, **185**, 1747–1758.

38 W. Li, L. Lindsay, D. A. Broido, D. A. Stewart and N. Mingo, *Phys. Rev. B Condens. Matter*, 2012, **86**, 174307.

39 A. M. Ganose, J. Park, A. Faghaninia, R. Woods-Robinson, K. A. Persson and A. Jain, *Nat. Commun.*, 2021, **12**, 2222.

40 G. K. Madsen, J. Carrete and M. J. Verstraete, *Comput. Phys. Commun.*, 2018, **231**, 140–145.

41 V. Wang, N. Xu, J.-C. Liu, G. Tang and W.-T. Geng, *Comput. Phys. Commun.*, 2021, **267**, 108033.

42 L. Yu and A. Zunger, *Phys. Rev. Lett.*, 2012, **108**, 068701.

43 I. Caño, A. Navarro-Güell, E. Maggi, A. Gon Medaille, D. Rovira, A. Jimenez-Arguijo, O. Segura, A. Torrens, M. Jimenez and C. López, *Small*, 2025, e05430.

44 R. S. Nielsen, Á. L. Álvarez, A. G. Medaille, I. Caño, A. Navarro-Güell, C. L. Álvarez, C. Cazorla, D. R. Ferrer, Z. J. Li-Kao and E. Saucedo, *J. Mater. Chem. A*, 2025, **13**, 31727–31739.

45 B. Wan, Z. Gao, X. Huang, Y. Yang, L. Chen, Q. Wang, C. Fang, W. Shen, Y. Zhang and H. Ma, *ACS Appl. Energy Mater.*, 2022, **5**, 9549–9558.

46 P. Acharyya, K. Pal, A. Ahad, D. Sarkar, K. S. Rana, M. Dutta, A. Soni, U. V. Waghmare and K. Biswas, *Adv. Funct. Mater.*, 2023, **33**, 2304607.

47 P. Rentzeperis, *Prog. Cryst. Growth Charact. Mater.*, 1991, **21**, 113–138.

48 E. Wlaźlak, A. Blachecki, M. Bisztyga-Szklarz, S. Klejna, T. Mazur, K. Mech, K. Pilarczyk, D. Przyczyna, M. Suchecki and P. Zawal, *Chem. Commun.*, 2018, **54**, 12133–12162.

49 C. Fong and F. Wooten, Experimental and Theoretical Study of the Feasibility of the Gunn Effect in BiSCl, BiSBr, BiSI, BiSeI, BiSeBr and BiSeCl, 1981.

50 P. Govindaraj, H. Kim and K. Venugopal, *J. Mater. Chem. C*, 2025, **13**, 13986–14000.

51 F. Mouhat and F.-X. Coudert, *Phys. Rev. B*, 2014, **90**, 224104.

52 M.-M. Zhong, X.-Y. Kuang, Z.-H. Wang, P. Shao, L.-P. Ding and X.-F. Huang, *J. Phys. Chem. C*, 2013, **117**, 10643–10652.

53 S. Yang, H. Shi, Y. Hu, J. Si, C. Chen, J. Yang, H. Qu, X. Hu, F. Zhang and S. Zhang, *J. Phys. Chem. Lett.*, 2024, **15**, 5721–5727.

54 S. Li, Photoelectric Behavior and Photovoltaic Performance of Bismuth Chalcohalides, PhD thesis, Kagawa University Publication, 2021.

55 A. Das, K. Debnath, I. Maria, S. Das, P. Dutta, D. Swain, U. V. Waghmare and K. Biswas, *J. Am. Chem. Soc.*, 2024, **146**, 30518–30528.

56 Z. Chen, H. Ming, Z. Li, S. N. Girard, C. D. Morris, W. Guo, M. Wu, Y. Yu, C. Wolverton and Z. Z. Luo, *Angew. Chem.*, 2025, **137**, e202501667.

57 R. Wu and A. M. Ganose, *J. Mater. Chem. A*, 2023, **11**, 21636–21644.

58 G. C. La Rocca, *Thin Films Nanostruct.*, 2003, **31**, 97–128.

59 M. Bokdam, T. Sander, A. Stroppa, S. Picozzi, D. Sarma, C. Franchini and G. Kresse, *Sci. Rep.*, 2016, **6**, 28618.

60 X.-J. Wu, Y.-F. Ding, B. Liu, J.-L. Yang and M.-Q. Cai, *Appl. Phys. Lett.*, 2022, **121**, 211103.

61 D. Zhang, B. Wang, Y. Gan, J. Zhou and Z. Sun, *J. Phys. Chem. C*, 2024, **128**, 1582–1590.

62 L. Yu, R. S. Kokenyesi, D. A. Keszler and A. Zunger, *Adv. Energy Mater.*, 2013, **3**, 43–48.

This journal is © The Royal Society of Chemistry 2026

J. Mater. Chem. A, 2026, **14**, 10694–10707 | **10707**